PAPER

Check for updates

Spatio-temporal evolution of laser ablation W plasma under low-pressure Ar gas and Ar plasma ambients†

Boliang Men, Cong Li, [iD] * Qi He, Hongmin Qu, Shiming Liu, Longfei Li, Huace Wu, Zhonglin He, Jielin Shi, Ding Wu, [iD] Ran Hai, [iD] Xingwei Wu and Hongbin Ding [iD]

Understanding the spatio-temporal evolution of laser ablation plasma under low-pressure ambients is a crucial area of study in the field of laser-induced breakdown spectroscopy (LIBS). In this work, LIBS combined with plasma imaging was employed to diagnose the spatio-temporal evolution of laser ablation W plasma under Ar gas ambient and continuous Ar plasma ambient with low-pressure conditions. Results revealed that laser ablation W plasma under Ar plasma ambient exhibited high radiative recombination loss and radiative thermal bremsstrahlung loss in the early stages of spatio-temporal evolution. This led to an increased continuous radiation background and W II signal intensity. It was found that the electron temperature initially exhibited a brief decline, followed by an increase, and then decreased gradually. This resulted in a temporary temperature drop caused by the inertia of plasma expansion, which was quickly compensated by the recompression of the shockwave layer. Plasma imaging results revealed plume splitting, plume sharpening, and plume turbulence in laser ablation W plasma under Ar gas ambient. The front position and area of the plasma plume under Ar gas ambient and Ar plasma ambient were compared. In the later stages of temporal evolution, the plume area of the plasma could be described using a drag model. Thus, this study provides new insights into the physical mechanisms of laser ablation W plasma under different background ambients, which is important for the real-time diagnostics of wall materials by LIBS during tokamak discharges.

1 Introduction

During the operation of a tokamak device, plasma wall interactions (PWI) lead to significant changes in the elemental composition of plasma-facing materials (PFMs).[1] Lifetime of the first wall and the retention rate of tritium (T) in future tokamak devices would be critical factors for their safety and economic performance.[2–5] For tokamak devices, a real-time and *in situ* diagnostic technique for material deposition and fuel retention on PFMs is necessary.[6,7] Laser-induced breakdown spectroscopy (LIBS) is a non-contact, *in situ*, on-line elemental analysis technique that enables the rapid detection of a wide range of elements in real-time, wherein a pulsed laser beam produces an outwardly expanding plasma when it ablates the surface of the sample. Different material elements emit transition spectral peaks at various wavelengths owing to their different electronic energy levels in the plasma. Information about the material components can be obtained using a spectrometer by observing the line radiation emitted by the excited plasma.[8–10] LIBS has a wide range of applications and has been successfully used to diagnose the condition of first wall materials in tokamak devices such as EAST.[11–14] During tokamak operations, such as discharge and wall conditioning, PFMs are exposed to different background pressures and ambient conditions. Different background ambient conditions can affect the dynamic expansion of laser ablation plasma, thus impacting the sensitivity and quantitative accuracy of LIBS measurements.

Laser ablation plasma is a transient evolution plasma with characteristic spectral peak intensity and plasma parameters (electron temperature (T_e) and electron density (n_e)), exhibiting a significant temporal and spatial inhomogeneity. Under the low-pressure environment of tokamak devices, the spatio-temporal evolution of the laser ablation plasma is more complex owing to the weaker interaction with background gas and faster expansion of plasma. For example, S. S. Harilal *et al.* investigated the expansion features of ultrafast laser-generated nanoparticle plumes in vacuum. ICCD fast-gated images showed two distinct features of component expansion generated by W plasma and nanoparticle plumes separated in time. Compared to low-*Z* materials (*e.g.*, Si), ultrafast laser ablation of high-*Z* materials such as W provides significantly higher nanoparticle yield.[15] Zhao *et al.* studied the spatio-temporal

Key Laboratory of Materials Modification by Laser, Ion, and Electron Beams (Ministry of Education), School of Physics, Dalian University of Technology, Dalian, 116024, People's Republic of China. E-mail: cli@dlut.edu.cn

evolution of laser ablation plasma on the first wall materials and provided optimum LIBS diagnostic design for the *in situ* diagnosis of the first wall under EAST tokamak environment.[16] Wu *et al.* employed fast photography and time- and space-resolved optical emission spectroscopy to systematically study laser-ablated W plasma properties at a low-pressure condition. The time-of-flight dynamics of the laser-induced W plasma presented four time-scales of plasma processes including prompt electron emission, continuum radiation, and ionic and atomic emission.[17] Wu *et al.* investigated the effect of gas pressure on the plume expansion and spectral emission of nanosecond laser-induced plasma of the W wall material. The plasma parameter change and laser ablation depth reduction were observed due to ambient gas confinement and enhanced plasma shielding.[18]

Apart from the significant influence of background pressure on laser ablation plasma, the ambient gas is also strongly correlated with the interaction between the laser and material during the ablation process. The spatio-temporal evolution characteristics of laser ablation plasma vary significantly in different ambient gases. During tokamak operation, impurity injection is commonly used for wall cleaning or divertor detachment.[19–23] The influence of ambient gas on laser ablation plasma has also attracted extensive attention from researchers. For example, Iida *et al.* observed that the LIBS signal intensity was higher in the Ar environment than in the He environment, while the plasma temperature decreased at a lower rate in Ar environment than in He environment.[24] Mao *et al.* found that plasma expansion in Ar and He is significantly different. The laser is absorbed by the compressed gas layer when the ambient gas ionization is low. This changes the plasma morphology, which in turn affects the signal intensity of LIBS.[25] Similar results were found in previous reports,[26–28] where the highest signal intensity was found in Ar environment, followed by Ne, air, and He.

LIBS exhibits excellent real-time and *in situ* diagnostic capabilities, enabling real-time elemental analysis of wall surfaces during long-pulse discharges in tokamak devices. During tokamak discharges, laser ablation plasma interacts with the background ambient plasma, especially in divertor detachment experiments where the divertor targets are often in a relatively high-pressure background plasma ambient. The background ambient plasma significantly influences the expansion process of laser ablation plasma. In the TEXTOR device, the interaction between laser ablation plasma and the background boundary plasma during discharges was studied.[29–31] Philipps *et al.* found that the volume of laser ablation plasma significantly increased in the edge plasma of the TEXTOR device.[32] Tokar *et al.* found that the ionization of ablated particles supplied additional electrons and increased plasma density. Energy losses in the excitation and ionization of the ablated particles, as well as the thermalization of the generated electrons, lead to a drop in the electron temperature.[33] Oelmann *et al.* used a high-speed camera to detect D_α radiation spatial and time-resolved radiation images of laser ablation plasma on the EAST device. A significant increase in

the size of laser ablation plasma in the edge plasma of the tokamak was found.[34]

Although preliminary experimental studies on the evolution behavior of laser ablation plasma in background plasma have been conducted on TEXTOR and EAST devices, the systematic spatio-temporal evolution patterns and mechanisms have not yet been reported. Generating plasma with plasma parameters similar to those of the edge plasma of tokamak devices to irradiate materials in the laboratory is the most important means of studying PWI. Linear plasma devices based on cascaded arc plasma source (CAPS) technology can generate large-area plasma beams characterized by high density, high ion flux, and high heat flux.[35–37] W is the most important wall material in tokamak devices. In this work, we irradiate W samples using Ar plasma generated by CAPS to study the evolution process of laser ablation W plasma under Ar plasma ambient. By comparing the spatio-temporal evolution behavior of laser ablation plasma under Ar gas and Ar plasma ambients, we aim to reveal the interaction mechanisms between laser ablation plasma and background plasma ambient. This study provides important experimental references for the real-time diagnostics of wall materials during tokamak discharges.

2 Experimental setup

The experimental system consists of four main parts: laser ablation system, signal collection system, plasma imaging system, and cascaded arc plasma source (CAPS) system. The schematic of the system is shown in Fig. 1.

The laser ablation system comprises an Nd:YAG laser (wavelength 1064 nm, pulse width 8 ns, maximum laser energy 110 mJ, CFR200 Quantel), optical components, and pure W targets (99.5% purity, Taibai Tungsten Products Factory, China). The laser pulse was focused onto the pure W targets in the vacuum chamber through a plano-convex lens (50.8 mm in diameter, 500 mm focal length) and a right-angle prism, producing a laser ablation W plasma. In this experiment, the laser energy was 100 mJ, and the laser energy density was estimated to be approximately 25.6 J cm^{-2} based on the contour of the laser ablation crater.

The signal collection system consists of a linear array of optical fibers, a signal-collected lens, and a spectrometer with an intensified charge-coupled device (ICCD) detector. The optical emission from the laser ablation W plasma was collected by a plano-convex lens (diameter 50.8 mm, focal length 75 mm) oriented parallel to the plasma. The plasma image was reduced by approximately 4 times, and the plasma optical emission was vertically guided into a linear array of optical fibers (comprising 20 fibers, each with a diameter of 300 μm). The fiber collection range was approximately 24 mm, allowing simultaneous recording of optical emission from 20 positions within the W plasma in a single measurement. The spatial resolution was ~1.2 mm on the plasma. The output end of the array fiber was vertically positioned at the entrance slit (70 μm) of the spectrometer (SR750, ANDOR) with a grating of 1200 lines per mm. The spectrometer was coupled with an ICCD (iStar 340T, ANDOR), which was connected to a computer for real-time

This journal is © The Royal Society of Chemistry 2025

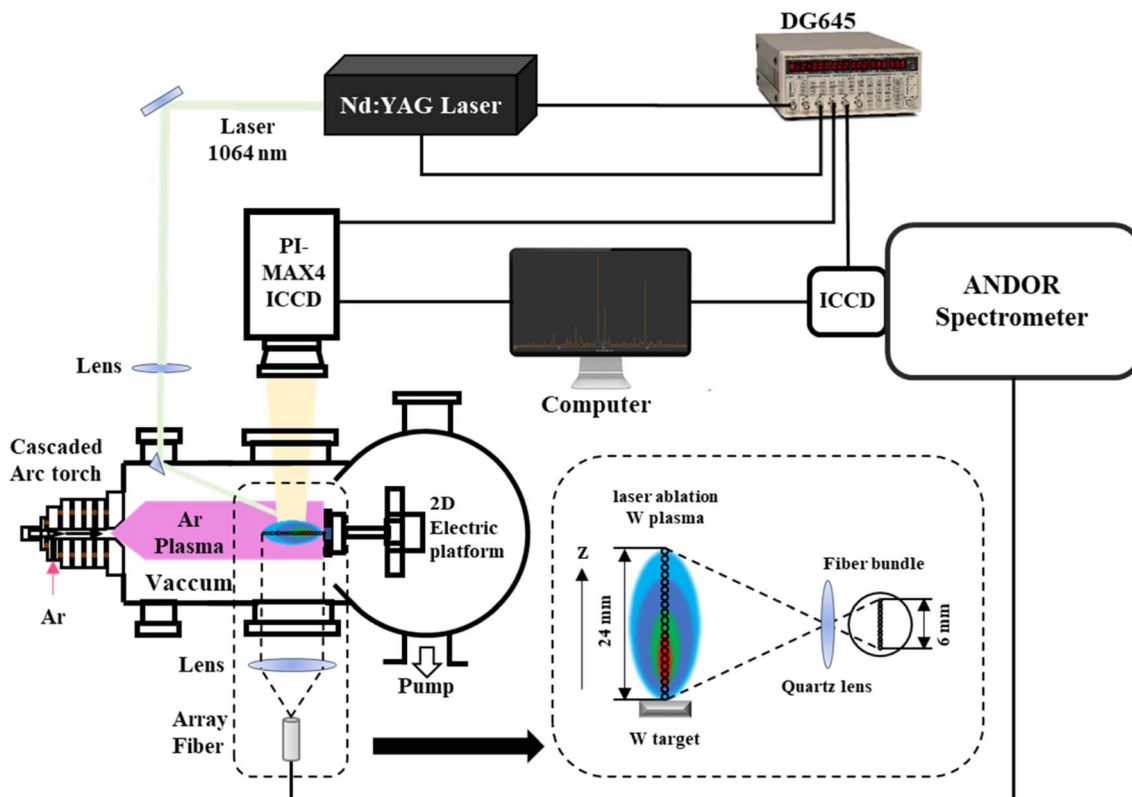*J. Anal. At. Spectrom.*, 2025, **40**, 762–774 | **763**

Fig. 1   Schematic of the laser ablation W plasma system.

acquisition of the spatio-temporal evolution of W plasma at different delays. The gate width for the spectral acquirement was 0.2 μs. The delay times were varied from 0 to 12.5 μs.

The plasma imaging system consists of an ICCD camera (PI-MAX4, Princeton Instruments) with a narrowband filter (center wavelength 430 nm, bandwidth 10 nm, RAYAN Optics). This setup recorded the expansion process of the laser ablation W plasma in the wavelength range from 425 nm to 435 nm using a camera. The delay times of the camera were varied from 0.05 μs to 3.05 μs with a step of 0.03 μs. The corresponding gate widths were varied from 3 ns to 303 ns with an increased step of 3 ns. According to our experience in previous plasma imaging experiments, the gate width is too long in the early stage of plasma evolution, leading to the overexposure of plasma image intensity. At the late stage of plasma evolution, the gate width is too short and will not result in a complete plasma evolution image. Therefore, we set the gate width increase step to 10% of the delay times increase step to get a complete plasma evolution image with better quality.

The cascaded arc plasma source system consists of CAPS (discharge gas: Ar gas), a vacuum chamber (modularly adjustable from 0.5 m to 3 m), and a vacuum pump assembly (WA251, SV100B, Leybold Vacuum). The real-time dynamic gas pressure inside the vacuum chamber during Ar gas flow was accurately measured using a high-precision thin film gauge (CMR361, Pfeiffer). CAPS operated with an adjustable working current from 60 A to 120 A and generated Ar plasma with a diameter of more than 10 cm and length of more than 1 m, which can cover

the size of LIBS plasma, with a steady-state run time of more than 1 hour. The electron density can reach 10^{20} m^{-3}, with an electron temperature of approximately 0.5 eV, ion flux of about 4.5×10^{23} m^{-2} s^{-1}, and heat flux of approximately 1 MW m^{-2}.[38,39] Thermal loads on the surface of the sample cause the sample temperature to increase, and the thermocouple on the back of the sample measures the sample temperature till about 500 °C.

A digital delay generator (DG645, Stanford) was used to synchronously control the triggering of the Nd:YAG laser, data acquisition of the spectrometer, and imaging of the camera. This setup enabled the investigation of the spatio-temporal evolution characteristics of laser ablation W plasma at low-pressure conditions, both under Ar gas ambient and Ar plasma ambient. The W samples were mounted on a 2D electric platform and can be moved during the experiment to prevent the ablation crater effect. The first 10 laser shots were used for surface cleaning. 60 spectra were averaged for each condition to reduce the fluctuation of plasma emission spectrum signals. The background pressure was 280 Pa in the vacuum chamber for Ar gas and Ar plasma ambients.

3   Results and discussion

3.1   Temporal evolution of spectral intensity laser ablation W plasma

Fig. 2 compares typical space-integrated spectra in the 420 nm to 440 nm wavelength range of laser ablation W plasma under
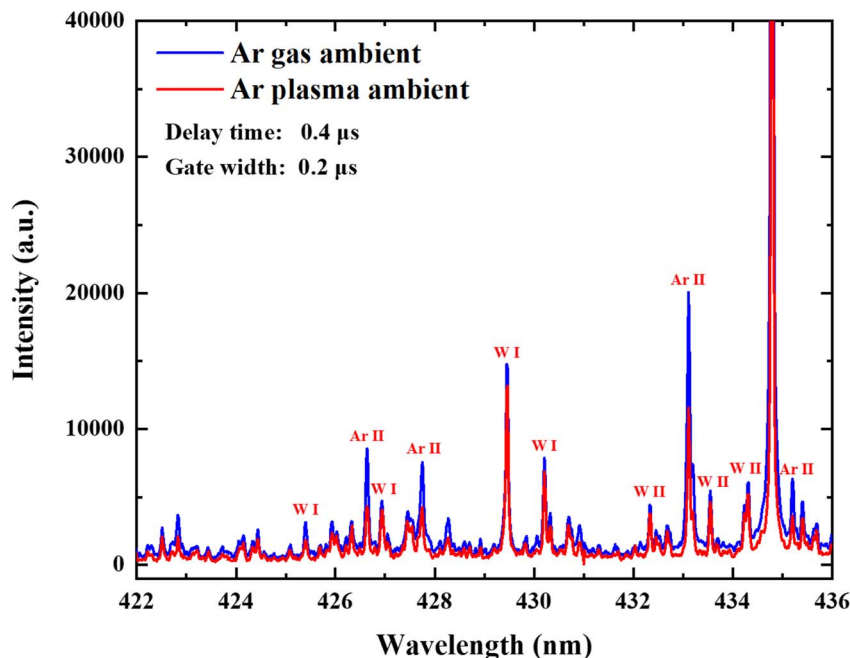
Fig. 2 Comparison of typical space-integrated spectra of W plasma under Ar gas ambient and Ar plasma ambient.

Ar gas ambient and Ar plasma ambient. The space-integrated spectra were obtained by averaging 20 spectra from 20 fibers. To study the effects of Ar gas ambient and Ar plasma ambient on the spatio-temporal evolution characteristics of laser ablation W plasma, it is essential to select the characteristic spectral peaks corresponding to W and Ar for analysis. The selection of characteristic spectral peaks should fully consider multiple influencing factors, such as whether different characteristic spectral peaks overlap, self-absorption effect of spectral peaks, and relative intensity of the spectral peaks. Considering these factors, W I 429.46 nm, W II 433.56 nm, continuous radiation background, and Ar II 433.12 nm were selected as the analytical spectral peaks for studying the spatio-temporal evolution characteristics of laser ablation W plasma. The intensity of continuous radiation background was obtained by the average intensity of 10 pixels near 430 nm.

Fig. 3 presents the space-integrated spectra of laser ablation W plasma at different delay times under Ar gas ambient and Ar plasma ambient. During the formation and expansion of the W plasma, the optical emission of the plasma changes continuously with increasing delay time, exhibiting complex physical processes such as excitation/ionization, recombination radiation, and de-excitation between the laser ablation W plasma and the background Ar gas. The signals of Ar II spectral peaks and the continuous radiation background appear almost simultaneously, indicating that the excitation and ionization of the background Ar gas occur almost simultaneously with the laser ablation W plasma. As the delay time increases, the W II spectral signals gradually appear, while the Ar II spectral signals disappear. With a further increase in delay time, W I spectral signals gradually dominate, W II spectral signals disappear, and the duration of W I spectral signals is significantly longer than that of W II.

Fig. 4 compares the temporal evolution of the space-integrated signal intensities of W plasma of the continuous radiation background, Ar II, W II, and W I under Ar gas ambient and Ar plasma ambient. With increasing delay time, the signals of Ar II and continuous radiation background reach their maximum intensity at about 0.2 μs. The optical emission processes of W II and W I follow those of Ar II and the continuous radiation background, reaching their peak signal intensity at 0.3 μs and 0.4 μs, respectively. The signal intensity of Ar II and the continuous radiation background are lower under Ar plasma ambient. The continuous radiation background signal disappears after 0.4 μs, while the Ar II signal gradually disappears after 1 μs. Under the Ar plasma ambient, the signal intensity of W II is higher before 0.2 μs. After 0.4 μs, there is a noticeable difference in the W II signal intensity between the Ar gas ambient and Ar plasma ambient. At about 0.8 μs, the signal intensity shows a brief increase and then rapidly decreases, with the W II signal intensity under the Ar plasma ambient decreasing faster, disappearing after 3.5 μs. The W I signal intensity shows a clear distinction before 0.3 μs and after 1.5 μs, which is stronger under Ar gas ambient. After 2 μs, the W I signal intensity initially increases and then decreases, maintaining a relatively high intensity at about 12.5 μs. In contrast, under Ar plasma ambient, the W I signal intensity continues to decline after 1.5 μs and disappears after 7.5 μs.

3.2 Temporal evolution of plasma parameters

The electron density of the space-integrated laser ablation W plasma was calculated using the Stark broadening method. As shown in eqn (1),

$$w_{\text{Stark}} = 2\left(\frac{n_{\text{e}}}{10^{16}}\right)w \tag{1}$$

This journal is © The Royal Society of Chemistry 2025

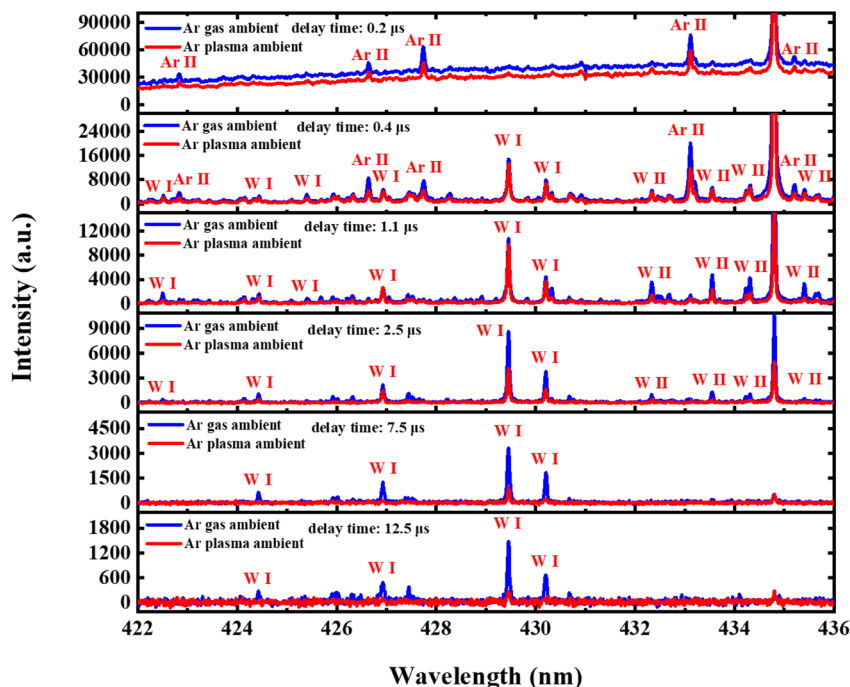*J. Anal. At. Spectrom.*, 2025, **40**, 762–774 | **765**

JAAS

Fig. 3 Comparison of space-integrated spectra of W plasma at different delay times under Ar gas ambient and Ar plasma ambient.

w_{Stark} is the full width at half maximum (FWHM) of the spectral peak, and w is the electron collision parameter.[40,41] In LIBS experiments, Stark broadening is usually more significant than the broadening caused by other mechanisms. The Doppler broadening can be neglected compared to Stark broadening, especially for the high-Z element such as W. Therefore, the spectral peak broadening observed in plasma spectroscopy results from both Stark broadening and instrumental broadening. During the collection of optical emission spectra, light passing through the slit of the spectrometer will have a certain width and will undergo diffraction, leading to some broadening known as instrumental broadening, which is measured using a standard Ar–Hg lamp and is determined to be of Gaussian shape, while the Stark broadened shape is Lorentzian. Therefore, the peak shape directly obtained from the spectrometer is a Voigt profile, which is a convolution of Gaussian and Lorentzian profiles. W I (429.46 nm) is chosen for electron density measurement. By deconvolution of the Voigt function, the Lorentzian FWHM obtained is w_{Stark}. Substituting w_{Stark} into eqn (1) yields the electron density n_{e}.

It is generally accepted that when the electron density and electron temperature meet certain conditions, the plasma can establish a local transient thermodynamic equilibrium, known as local thermal equilibrium (LTE). When the laser ablation plasma is in a state of LTE, the electron temperature of the plasma can be studied. The electron temperature can be calculated using the Boltzmann slope method and the Saha–Boltzmann slope method. Under LTE conditions, the optical emission intensity I_{ij} of a specific transition wavelength λ_{ij} from a higher energy level E_i to a lower energy level E_j is given by eqn (2).

$$I_{ij} = A_{ij}n\frac{hc}{\lambda_{ij}}\left(\frac{g_j}{U(T)}\right)e^{-E_i/k_B T} \quad (2)$$

After linearizing eqn (2), the electron temperature T of the plasma can be calculated using the atomic Boltzmann slope method as follows.

$$\ln\left(\frac{I_{ij}\lambda_{ij}}{A_{ij}g_j}\right) = -\frac{E_i}{k_B T} + \ln\left(\frac{nhc}{U(T)}\right) \quad (3)$$

In eqn (3), which takes the form $y = ax + b$, the plasma temperature T can be obtained from the slope $a = -\dfrac{1}{k_B T}$. The Boltzmann slope method uses characteristic atomic spectral peaks, where the energy differences between atomic levels are relatively small, leading to relatively large calculation errors. On the other hand, the Saha–Boltzmann slope method simultaneously utilizes atomic spectral peaks and ion spectral peaks. The energy differences between atomic levels and excited ion levels are significantly larger, which can enhance calculation accuracy.[42,43] The expression for the ion Boltzmann slope method is as follows.

$$\ln\left(\frac{I_{ij}^{\text{II}}\lambda_{ij}^{\text{II}}}{A_{ij}g_j}\right) = -\frac{E_i}{k_B T} + \ln\left(\frac{n^{\text{II}}hc}{U^{\text{II}}(T)}\right) \quad (4)$$

In eqn (4), superscript II represents singly ionized ions. According to the Saha equation, the ratio of the number of atoms to singly ionized ions is given as follows.

$$\frac{n^{\text{II}}}{n} = 2\left(\frac{U^{\text{II}}(2\pi m_e kT)^{\frac{3}{2}}}{nn_e h^3}\right)\exp\left(-\frac{E_{\text{ion}} - \Delta E}{k_B T}\right) \quad (5)$$
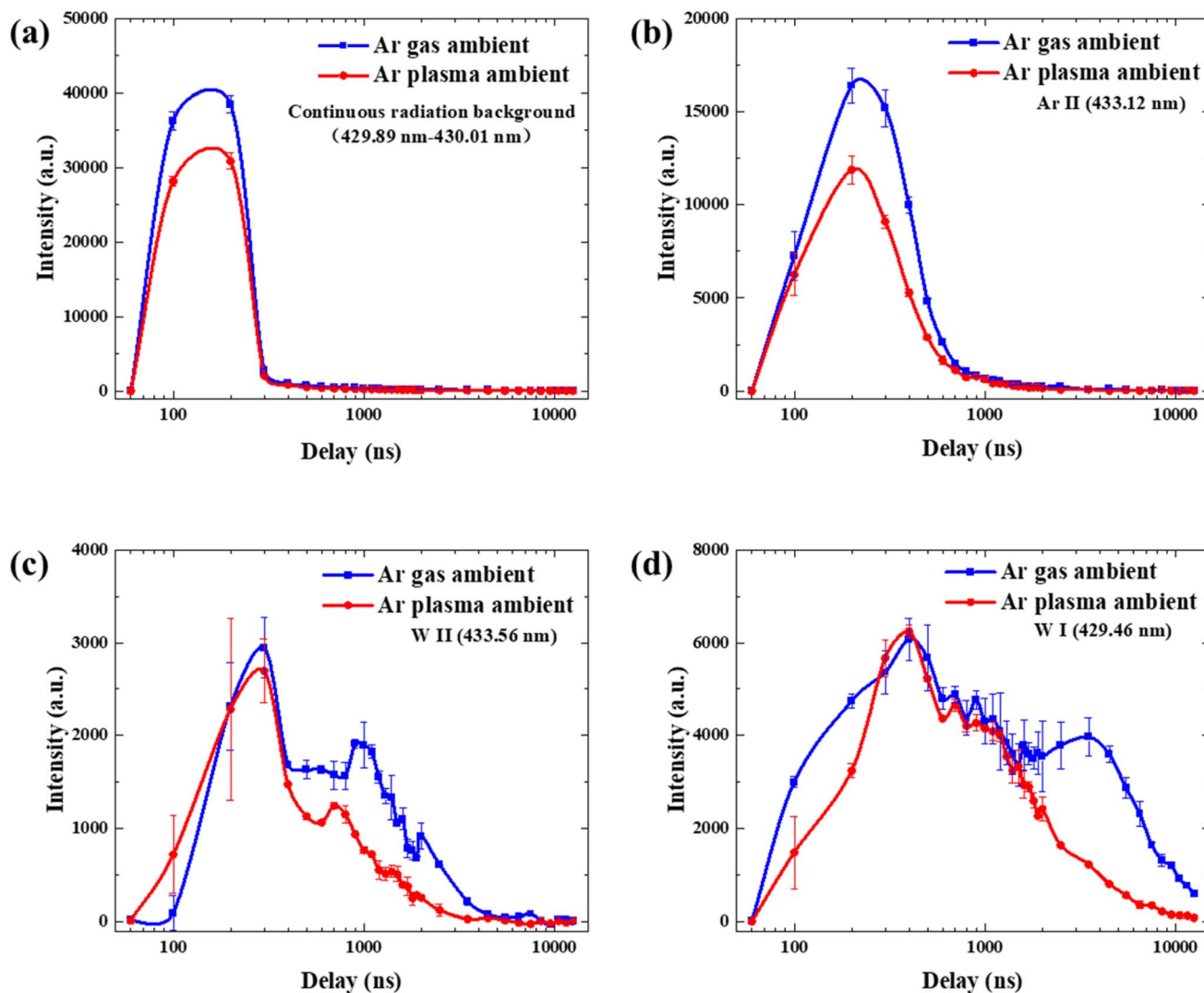
Fig. 4 Comparison of the temporal evolution of the space-integrated signal intensity of W plasma under Ar gas ambient and Ar plasma ambient: (a) continuous radiation background; (b) Ar II (433.12 nm); (c) W II (433.56 nm); (d) W I (429.46 nm).

In eqn (5), m_e is the electron mass, n_e is the electron density, and E_{ion} is the first ionization energy of the atom. ΔE represents the ionization energy correction value, which is approximately 0.1 eV. By substituting eqn (5) into eqn (4) and rearranging, we obtained the Saha–Boltzmann slope expression as eqn (6).

$$\ln\left(\frac{I_{ij}^{II}\lambda_{ij}^{II}}{A_{ij}g_j}\right) - \ln\left(\frac{2(2\pi m_e kT)^{\frac{3}{2}}}{n_e h^3}\right) = -\frac{E_i + E_{ion} - \Delta E}{k_B T} + \ln\left(\frac{n^{II}hc}{U^{II}(T)}\right)$$

(6)

In the Saha–Boltzmann plot, the horizontal and vertical coordinates for atoms are the same as those in the Boltzmann slope method. For ions, the vertical coordinate is expressed as follows: $\ln\left(\frac{I_{ij}^{II}\lambda_{ij}^{II}}{A_{ij}g_j}\right) - \ln\left(\frac{2(2\pi m_e kT)^{\frac{3}{2}}}{n_e h^3}\right)$, where the horizontal

coordinate is $E_i + E_{ion} - \Delta E$. In the Saha–Boltzmann plot, the slope of the linear fit still represents the negative reciprocal of the electron temperature. The electron temperature T_e was calculated using the Saha–Boltzmann slope method. The necessary parameters for this calculation, including the transition probabilities A_{ij} and statistical weights g_j for the selected spectral peaks, are taken from the NIST database. These spectroscopic parameters are presented in Table 1.

A strong continuous radiation background at the initial stage of laser ablation on W samples makes it impossible to distinguish the W I and W II spectra. Therefore, the spectra after 0.3 µs were selected to study the temporal evolution of the space-integrated electron density and electron temperature of the W plasma under both Ar gas ambient and Ar plasma ambient. The results are shown in Fig. 5. It was found that the electron temperature initially exhibits a brief decline, followed by an increase, and then slowly decreases. This corresponds to a temporary temperature drop caused by the inertia of plasma

Table 1 Spectroscopic parameters of W

	λ (nm)	$g_k A_{ki}$ (10^6 s^{-1})	E_i (eV)	E_k (eV)
W I	424.44	15.2	0.771	3.691
W I	426.94	15.2	0.366	3.269
W I	429.46	62	0.366	3.252
W I	430.21	25	0.366	3.247
W II	433.56	3.73	2.355	5.213
W II	434.31	5.76	2.794	5.648

Table 2 Reactions involving Ar with W and electrons

Reaction	Reference
$Ar + e^- \rightarrow Ar^+ + e^- + e^-$	44
$Ar + e^- \rightarrow Ar^* + e^-$	44
$Ar^* + e^- \rightarrow Ar^+ + e^- + e^-$	44
$Ar^+ + e^- + Ar \rightarrow Ar + Ar$	48
$Ar + Ar \rightarrow Ar^* + Ar$	48
$Ar^* + Ar \rightarrow Ar^+ + Ar + e^-$	48
$Ar^* + Ar^* \rightarrow Ar^+ + Ar + e^-$	49
$Ar^+ + e^- \rightarrow Ar^{(*)} + h\nu$	50
$W + Ar^+ \rightarrow W^+ + Ar$	51
$W + Ar^* \rightarrow W^* + Ar$	52
$W + Ar^* \rightarrow W^+ + Ar + e^-$	53

expansion, which is quickly compensated by the recompression of the shockwave layer. The subsequent evolution shows a slow decline due to the insufficient collision frequency to maintain excitation equilibrium, reflecting the gradual de-excitation process of the W plasma.[44] When irradiated by Ar plasma, the W sample reaches a high temperature of approximately 500 °C. Previous LIBS experiments have shown that as the sample temperature increases, the optical emission intensity, electron temperature, and electron density of the laser ablation plasma significantly increase.[45–47] Under Ar plasma ambient, as the temperature of the W sample increases, the optical emission intensity of the laser ablation W plasma and the electron temperature decrease more rapidly. This indicates that the sample temperature has a minimal effect on the temporal evolution of the laser ablation W plasma, and the dominant factor is the strong interaction between the laser ablation W plasma and the Ar plasma.

3.3 Spatio-temporal evolution of spectral intensity

In the early stages of spatio-temporal evolution, the Ar gas breaks down prior to the formation of laser ablation W plasma. Ar gas breakdown influences the laser energy coupling to the W target, and Ar breakdown emission was observed in the laser ablation W plasma. Ar gas ambient enhances the analytical emission signal by improving the excitation efficiency of W

atoms by collision with excited photoionized Ar species.[26] Under Ar plasma ambient, neutral Ar atoms and excited Ar atoms dominate. As the laser ablation W plasma continues to expand in a vacuum, strong interactions between the W plasma and Ar gas/Ar plasma occur in the later stages of spatio-temporal evolution. The properties of the plasma and ambient environment determine the expansion dynamics of the plasma plume. The reactions involving Ar, Ar*, and Ar$^+$ with e$^-$, W, W* and W$^+$ under Ar gas ambient and Ar plasma ambient are shown in Table 2.

Fig. 6 compares the spatio-temporal evolution spectra of laser ablation W plasma under Ar gas ambient and Ar plasma ambient at different delay times and spatial collection positions. At a delay time of 0.2 μs, only the continuous radiation background and Ar II spectral peaks were observed, with the optical emission intensity decreasing as the plasma spatial collection position increases. Under Ar gas ambient, Ar II spectral peaks are detectable at all spatial collection positions. This indicates that the intense laser-plasma interaction produces a high-pressure kinetic zone with an extremely rapid expansion speed, exciting and ionizing the Ar gas. The
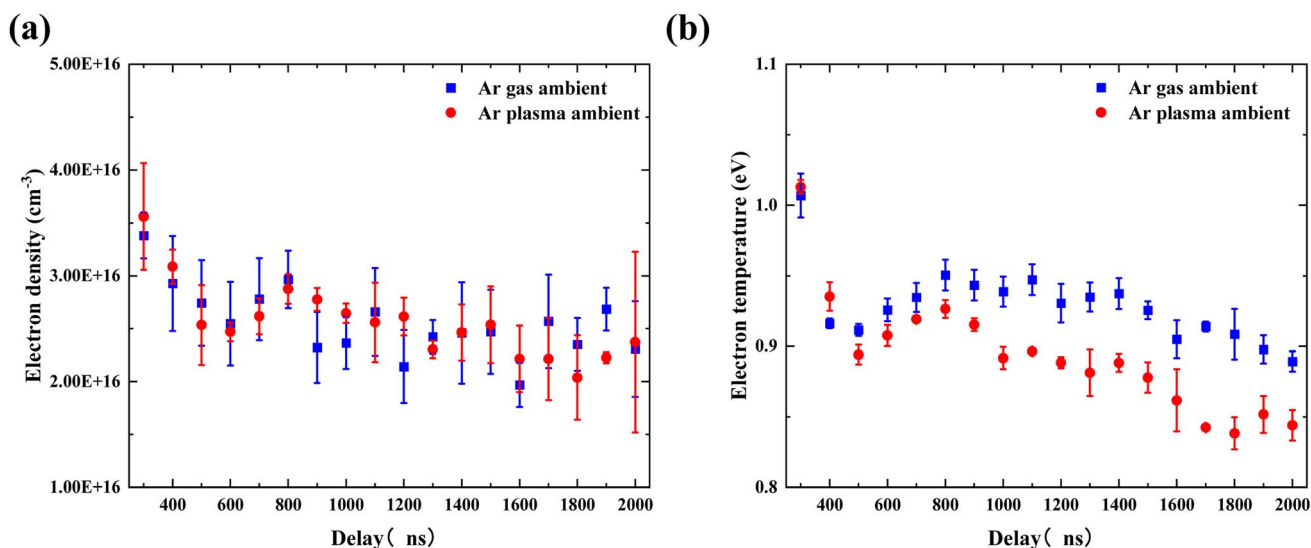

Fig. 5 Temporal evolution of space-integrated (a) electron density and (b) electron temperature of W plasma under Ar gas ambient and Ar plasma ambient.

768 | *J. Anal. At. Spectrom.*, 2025, **40**, 762–774
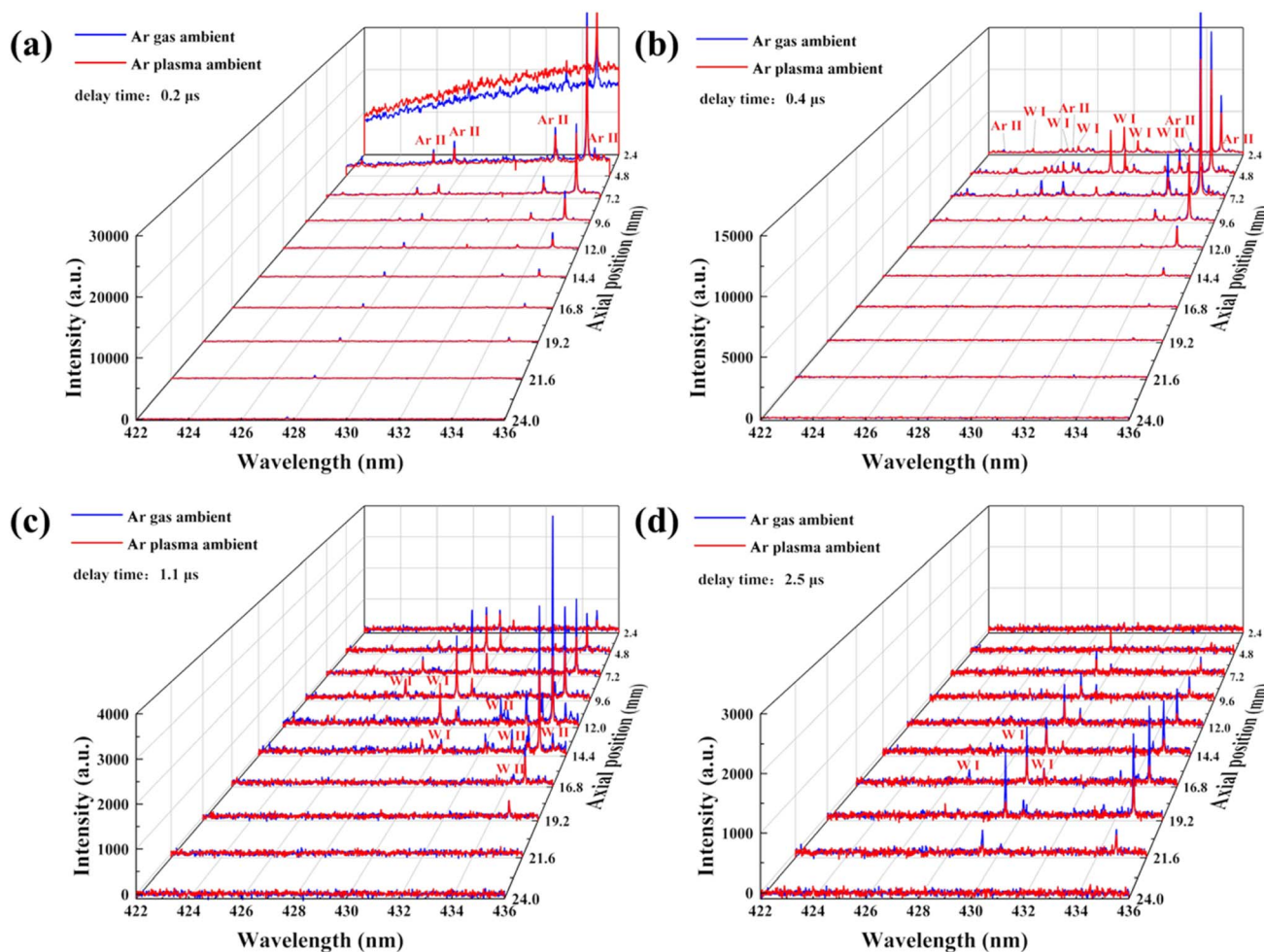
This journal is © The Royal Society of Chemistry 2025

Fig. 6 Comparison of the spatio-temporal evolution of W plasma spectra under Ar gas ambient and Ar plasma ambient. Delay time: (a) 0.2 μs; (b) 0.4 μs; (c) 1.0 μs; (d) 2.5 μs.

continuous radiation background disappears as the delay time increases to 0.4 μs, and W I and W II spectral peaks appear. The W plasma expands axially to approximately 9.6 mm, with the plasma core of about 7.2 mm. With a further increase in delay time to 1 μs, the Ar II spectral peaks disappear, and the W plasma expands to approximately 14.4 mm, with the plasma core moving axially to 12 mm. At a delay time of 2.5 μs, the W II spectral peaks disappear, and the W plasma expands to 21.6 mm. All spectral signals disappear before 4.8 mm, with the plasma core moving forward to approximately 19.2 mm.

The radiation involved in the spatio-temporal evolution of laser ablation W plasma includes radiative recombination and thermal bremsstrahlung radiation. The collision processes encompass excitation–deexcitation and ionization–

Table 3 Basic processes of radiation and collision involved in the spatio-temporal evolution of W plasma

Name	Reaction
Excitation–deexcitation under electron impact	$\mathrm{W}_i + \mathrm{e}^- \rightleftharpoons \mathrm{W}_{j>i} + \mathrm{e}^-$
	$\mathrm{W}_i^+ + \mathrm{e}^- \rightleftharpoons \mathrm{W}_{j>i}^+ + \mathrm{e}^-$
Excitation–deexcitation under heavy particle impact	$\mathrm{W}_i + \sum_{i,Z}\mathrm{W}_i^{Z+} \rightleftharpoons \mathrm{W}_{j>i} + \sum_{i,Z}\mathrm{W}_i^{Z+}$
	$\mathrm{W}_i^+ + \sum_{i,Z}\mathrm{W}_i^{Z+} \rightleftharpoons \mathrm{W}_{j>i}^+ + \sum_{i,Z}\mathrm{W}_i^{Z+}$
Ionization–recombination under electron impact	$\mathrm{W}_i + \mathrm{e}^- \rightleftharpoons \mathrm{W}_j^+ + 2\mathrm{e}^-$
	$\mathrm{W}_j^+ + \mathrm{e}^- \rightleftharpoons \mathrm{W}^{2+} + 2\mathrm{e}^-$
Ionization–recombination under heavy particle impact	$\mathrm{W}_i + \sum_{i,Z}\mathrm{W}_i^{Z+} \rightleftharpoons \mathrm{W}_j^+ + \mathrm{e}^- + \sum_{i,Z}\mathrm{W}_i^{Z+}$
	$\mathrm{W}_j^+ + \sum_{i,Z}\mathrm{W}_i^{Z+} \rightleftharpoons \mathrm{W}^{2+} + \mathrm{e}^- + \sum_{i,Z}\mathrm{W}_i^{Z+}$
Radiative recombination	$\mathrm{W}_i^{Z+} + \mathrm{e}^- \rightarrow \mathrm{W}_i^{(Z-1)+} + h\nu$
Thermal bremsstrahlung	$\mathrm{W}_i^{Z+} + \mathrm{e}^- \rightarrow \mathrm{W}_i^{Z+} + \mathrm{e}^- + h\nu$

This journal is © The Royal Society of Chemistry 2025

J. Anal. At. Spectrom., 2025, 40, 762–774 | 769

recombination under electron and heavy particle collisions.[50] The reaction processes are shown in Table 3.

Fig. 7 compares the spatio-temporal evolution of the signal intensities of W plasma of the continuous radiation background, Ar II, W II, and W I under Ar gas ambient and Ar plasma ambient. LIBS has strong continuous radiation background in the early stages of plasma evolution, and the main factors that produce strong continuous radiation background are thermal bremsstrahlung and radiative recombination. Thermal bremsstrahlung is produced by coulomb collisions of electrons with high kinetic energy with ions (or atoms) at high temperatures, resulting in a decrease in the kinetic energy of the electrons, which radiates excess energy as photons.[54] Prior to the delay of 0.4 μs, the intensity of the continuous radiation background increased and the Ar II signal intensity decreased in the Ar plasma ambient in the 2.4 mm collection region. Radiative recombination is produced when free electrons are captured by ions and recombined with ions to form neutral particles, and the excess energy is also radiated outward in the form of photons. By comparing the spatio-temporal evolution of W II and W I signal intensity under Ar gas ambient and Ar plasma ambient, the W II signal intensity increased in the Ar plasma ambient within the 2.4 mm collection area before a delay of 0.4 μs. The increase in the intensity of the continuous radiation background and the W II signal intensity indicate that in the early stages of spatio-temporal evolution, plasma radiative recombination loss and radiative thermal bremsstrahlung loss are higher under the Ar plasma ambient. After a delay time of 1 μs, there is a significant differentiation in the evolution of the W II and W I signal intensity. There is a noticeable enhancement in the W I signal intensity under Ar gas ambient. As the spatial collection position increases, the difference in the spatio-temporal evolution of the W I signal intensity between Ar gas ambient and Ar plasma ambient becomes more pronounced. This indicates that the enhancement of W I signal intensity under Ar gas ambient is mainly concentrated in the later stages of spatio-temporal evolution, corresponding to an increase in evolution time.
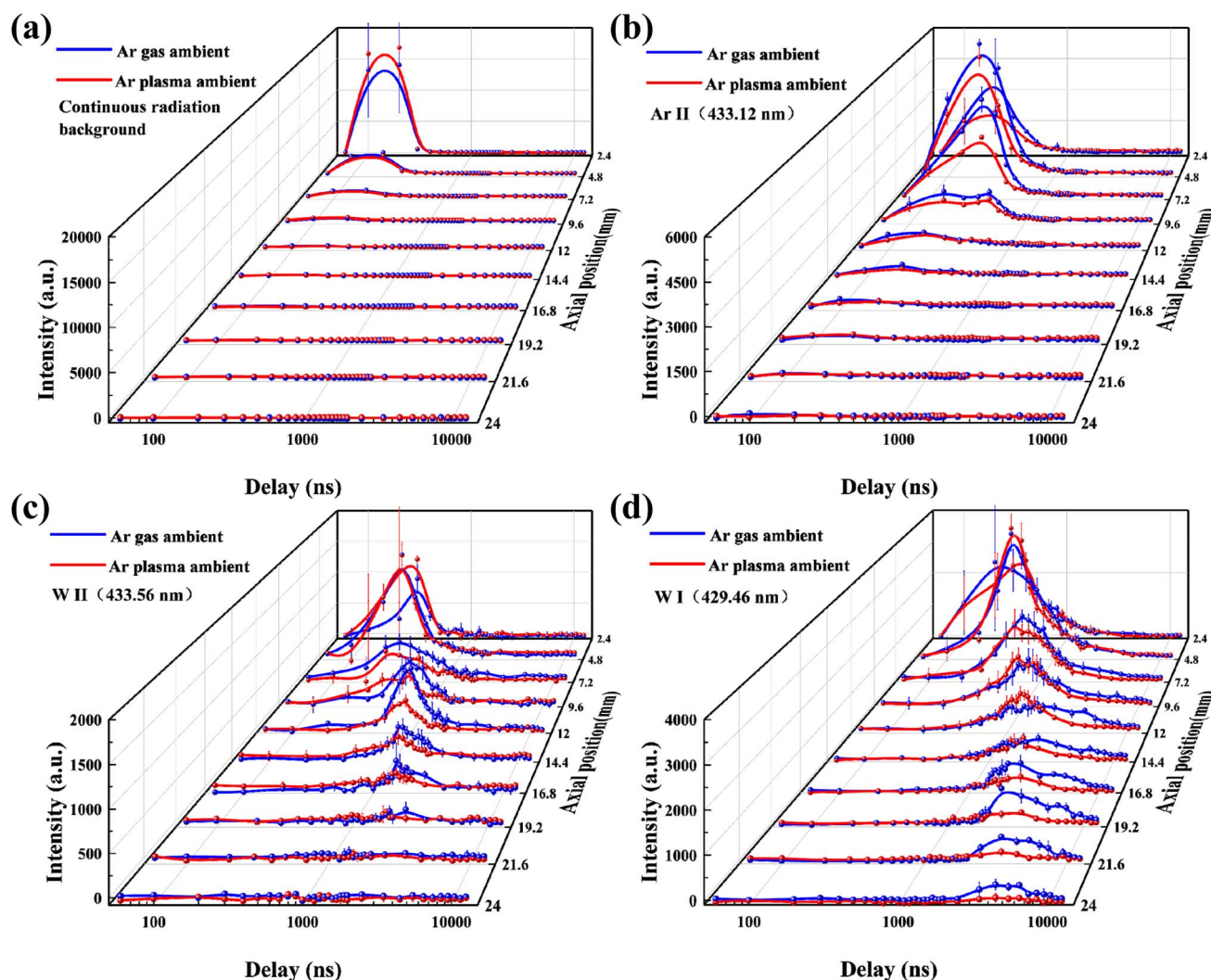

Fig. 7 Comparison of the spatio-temporal evolution of the signal intensity of W plasma under Ar gas ambient and Ar plasma ambient: (a) continuous radiation background; (b) Ar II (433.12 nm); (c) W II (433.56 nm); (d) W I (429.46 nm).

770 | *J. Anal. At. Spectrom.*, 2025, **40**, 762–774

This journal is © The Royal Society of Chemistry 2025

3.4 Dynamic evolution of the image of laser ablation W plasma

Fast photography by an ICCD camera during the temporal evolution of laser ablation W plasma provides images of the plasma plume interacting with the background ambient. It is crucial to study the temporal evolution of laser ablation W plasma under Ar gas ambient and Ar plasma ambient. Fig. 8 compares the temporal evolution of laser ablation W plasma imaged by the ICCD camera under Ar gas ambient and Ar plasma ambient. The expansion of the laser ablation W plasma produces a plasma plume. The influence of the ambient particles on the temporal evolution of the plasma plume includes: 1. strong collisions between the shock layer and Ar gas/Ar plasma, followed by collisions between the expanding W plasma and the shock layer, which increase the optical emission intensity of the W plasma; 2. formation of the shock front, where collisions between the shock layer and ambient particles constrain the plasma plume compared to vacuum.[55] The plasma plume detaches from the W surface after 50 ns, with plume splitting observed at about 140 ns. Fast-moving and slow-moving components form near the W surface, creating a contact boundary between the W plasma and the shock layer. During this intense collision process, the laser ablation W plasma transfers kinetic energy to the ambient particles, involving energy and momentum transfer processes such as ion–ion Coulomb scattering, ion-neutral collisions, and charge exchange,[55] with the plume splitting phenomenon persisting until ~320 ns.

Fig. 9 shows the comparison of the temporal evolution of the plume front position of the plasma and plume area of the plasma from laser ablation W plasma under Ar gas ambient and Ar plasma ambient. We integrated the plasma image in radial and axial directions, yielding a spectrum with 10% of the peak intensity as the boundary. The size of each pixel point is known, and the total number of pixel points within the boundary × length of each pixel point = the long and short axes A and B of the quasi-elliptical plasma expansion, which was approximated using the MATLAB program according to the elliptical area formula $S = \pi \times A \times (B/4)$ to calculate the plasma area. Under Ar gas ambient, the velocity of the plume front position decays more quickly and combines with the slow-moving component. As the plasma plume continues to expand, it experiences stronger spatial confinement, compressing it into shorter dimensions. This increases collisions and recombination, prolonging the plasma plume's optical emission intensity and leading to longer evolution under Ar gas ambient. The temporal relationship of the plasma plume front position follows $t^{0.458}$ under Ar gas ambient and $t^{0.516}$ under Ar plasma ambient. Under Ar plasma ambient, stronger collisions between the plasma plume and ambient particles result in a larger emission region, making the plasma plume appear larger, but the optical emission intensity decreases. It is also noted that in the earlier stage (<650 ns), the plume area of the plasma is almost linear, irrespective of both the Ar gas ambient and Ar plasma ambient. In the later stages of temporal evolution, the plume area of the plasma can be described by a drag model, which is given by

$$R = R_0(1 - e^{-\beta t}) \tag{7}$$

where R_0 and β are the plume stopping distance and deceleration coefficient, respectively. During this interaction phase between the laser ablation W plasma and the ambient particles, a significant portion of kinetic energy is converted to thermal energy, increasing the temperature of the ambient gas and radiation. Under Ar gas ambient, the fast-moving component of the plasma plume rapidly penetrates the ambient particles, with turbulence appearing in the slow-moving component of the
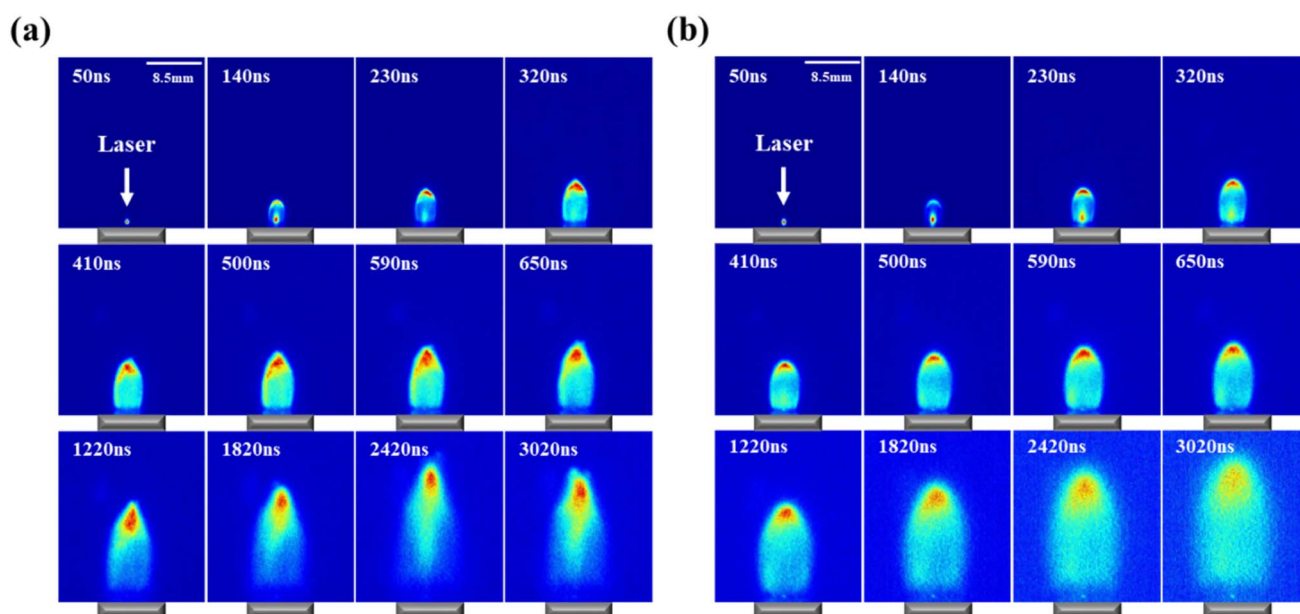

Fig. 8 Temporal evolution of laser ablation W plasma images under (a) Ar gas ambient and (b) Ar plasma ambient.
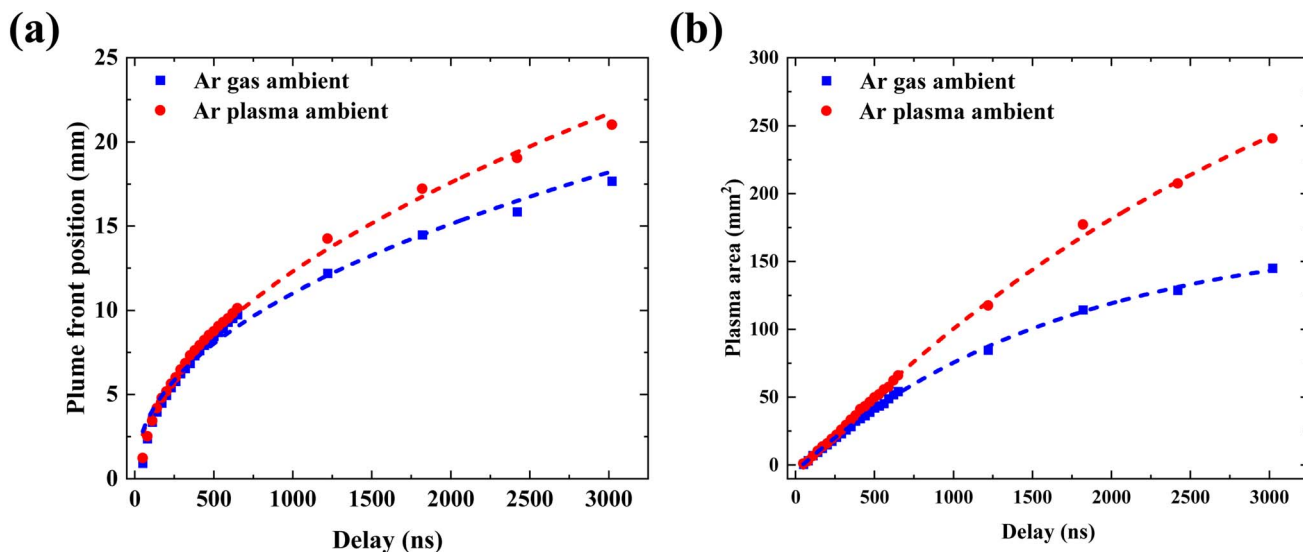
This journal is © The Royal Society of Chemistry 2025

J. Anal. At. Spectrom., 2025, 40, 762–774 | 771

(a)

(b)

Fig. 9 Temporal evolution of (a) plume front position and (b) plume area from images of laser ablation W plasma under Ar gas ambient and Ar plasma ambient.

plasma plume. At the same time, the low-pressure background leads to contraction of the interaction zone and compression of the plasma front. The plasma turbulence in the background gas originates from Rayleigh–Taylor (RT) instability, where the interface between the plasma and ambient atmosphere is perturbed due to RT instability.[56] Under Ar plasma ambient, only plume splitting and plume sharpening phenomena are observed, and no plasma turbulence is detected. The constraints on the plasma plume in the radial and axial directions are less, resulting in a larger plume diffusion area.

4 Conclusion

In this work, we employed LIBS combined with plasma imaging to compare and diagnose the spatio-temporal evolution of laser ablation W plasma under Ar gas ambient and Ar plasma ambient. LIBS studies reveal that laser ablation W plasma under Ar plasma ambient exhibits higher radiative recombination loss and radiative thermal bremsstrahlung loss in the early stages of spatio-temporal evolution, leading to increased continuous radiation background and W II signal intensity. The enhancement of the W plasma signal intensity under Ar gas ambient primarily occurs in the later stages of spatio-temporal evolution due to the strong interactions between W plasma and ambient particles, which extend the evolution time of W plasma. The temporal evolution of the space-integrated electron temperature of the W plasma under both Ar gas ambient and Ar plasma ambient was studied. It was found that the electron temperature initially exhibits a brief decline, followed by an increase, and then slowly decreases. This corresponds to a temporary temperature drop caused by the inertia of plasma expansion, which is quickly compensated by the recompression of the shockwave layer. Subsequent evolution shows a slow decline due to the insufficient collision frequency to maintain the excitation equilibrium, reflecting the gradual de-excitation

process of W plasma. Plasma imaging studies reveal the phenomena of plume splitting, plume sharpening, and plume turbulence in laser ablation W plasma under Ar gas ambient. Under the Ar plasma ambient, only plume splitting and plume sharpening phenomena are observed, and no plasma turbulence is detected. Under Ar gas ambient, the strong interaction zone between the laser ablation W plasma and ambient particles contracts more significantly, resulting in stronger spatial confinement of the plasma front. The position of plasma plume front R is proportional to $t^{0.458}$ under Ar gas ambient and the position of plasma plume front R is proportional to $t^{0.516}$ under Ar plasma ambient. As the plasma plume continues to expand, the front under the Ar gas ambient is constrained to a shorter dimension, which enhances collisions and recombination, thereby prolonging the evolution time of the plasma plume. It was also noted that in the earlier stage (<650 ns), the plume area of the plasma is almost linear, irrespective of both the Ar gas ambient and Ar plasma ambient. In the later stages of temporal evolution, the plume area of the plasma can be described by a drag model. This study provides new insights into the physical mechanisms of laser ablation W plasma under different background ambients, which is crucial for further understanding the spatio-temporal evolution characteristics of LIBS plasma.

Data availability

The data supporting this article have been included as part of the ESI.†

Author contributions

Boliang Men: methodology, data curation, investigation, writing – original draft. Cong Li: conceptualization, writing – review & editing, funding acquisition, supervision. Qi He: investigation. Hongming Qu: investigation. Shiming Liu:

772 | *J. Anal. At. Spectrom.*, 2025, **40**, 762–774

This journal is © The Royal Society of Chemistry 2025

investigation. Longfei Li: investigation. Huace Wu: investigation. Zhonglin He: investigation. Jielin Shi: investigation. Ding Wu: funding acquisition. Ran Hai: funding acquisition. Xingwei Wu: funding acquisition. Hongbin Ding: resources, funding acquisition, project administration.

Conflicts of interest

There are no conflicts to declare.

Acknowledgements

References

1 B. D. Wirth, K. D. Hammond, S. I. Krasheninnikov and D. Maroudas, *J. Nucl. Mater.*, 2015, **463**, 30–38.

2 D. E. Post and R. Behrisch, *Physics of Plasma-Wall Interactions in Controlled Fusion*, Springer Science & Business Media, 2013.

3 G. Janeschitz and I. J. J. o. N. M. Jct, *J. Nucl. Mater.*, 2001, **290**, 1–11.

4 A. Loarte, B. Lipschultz, A. S. Kukushkin, G. F. Matthews, P. C. Stangeby, N. Asakura, G. F. Counsell, G. Federici, A. Kallenbach and K. Krieger, *Nucl. Fusion*, 2007, **47**, S203.

5 J. Roth, E. Tsitrone, A. Loarte, T. Loarer, G. Counsell, R. Neu, V. Philipps, S. Brezinsek, M. Lehnen, P. Coad, C. Grisolia, K. Schmid, K. Krieger, A. Kallenbach, B. Lipschultz, R. Doerner, R. Causey, V. Alimov, W. Shu, O. Ogorodnikova, A. Kirschner, G. Federici, A. Kukushkin, E. P. T. Force, I. P. Team, E. Fusion and D. I. V. Itpa Sol, *J. Nucl. Mater.*, 2009, **390–91**, 1–9.

6 J. Karhunen, A. Hakola, J. Likonen, A. Lissovski, M. Laan, P. Paris and J. E. Contributors, *J. Nucl. Mater.*, 2015, **463**, 931–935.

7 D. Y. Zhao, C. Li, Z. H. Hu, C. L. Feng, Q. M. Xiao, R. Hai, P. Liu, L. Y. Sun, D. Wu, C. L. Fu, J. M. Liu, N. Farid, F. Ding, G. N. Luo, L. Wang and H. B. Ding, *Rev. Sci. Instrum.*, 2018, **89**, 073501.

8 D. A. Cremers and L. J. Radziemski, *Handbook of Laser-Induced Breakdown Spectroscopy*, John Wiley & Sons, 2013.

9 S. Musazzi and U. J. S. S. i. O. S. Perini, in *Laser-Induced Breakdown Spectroscopy Theory and Applications*, Springer Series in Optical Sciences, 2014, p. 182, https://link.springer.com/book/10.1007/978-3-642-45085-3.

10 J. P. Singh and S. N. Thakur, *Laser-induced Breakdown Spectroscopy*, Elsevier, 2020.

11 C. Li, D. Y. Zhao, Z. H. Hu, X. W. Wu, G. N. Luo, J. S. Hu and H. B. Ding, *J. Nucl. Mater.*, 2015, **463**, 915–918.

12 N. Gierse, B. Schweer, A. Huber, O. Karger, V. Philipps, U. Samm and G. Sergienko, *J. Nucl. Mater.*, 2011, **415**, S1195–S1198.

13 C. Grisolia, A. Semerok, J. M. Weulersse, F. Le Guern, S. Fomichev, F. Brygo, P. Fichet, P. Y. Thro, P. Coad, N. Bekris, M. Stamp, S. Rosanvallon and G. Piazza, *J. Nucl. Mater.*, 2007, **363**, 1138–1147.

14 Z. H. Hu, N. Gierse, C. Li, J. Oelmann, D. Y. Zhao, M. Tokar, X. Jiang, D. Nicolai, J. Wu, F. Ding, S. Brezinsek, H. B. Ding, G. N. Luo and C. Linsmeier, *Fusion Eng. Des.*, 2018, **135**, 95–101.

15 S. S. Harilal, N. Farid, A. Hassanein and V. M. Kozhevin, *J. Appl. Phys.*, 2013, **114**, 203302.

16 D. Y. Zhao, C. Li, Y. Wang, Z. W. Wang, L. Gao, Z. H. Hu, J. Wu, G. N. Luo and H. B. Ding, *Plasma Sci. Technol.*, 2018, **20**, 014022.

17 D. Wu, L. Y. Sun, J. M. Liu, X. Yu, R. Hai, C. L. Feng, Z. W. Wang and H. B. Ding, *Phys. Plasmas*, 2019, **26**, 013303.

18 D. Wu, L. Y. Sun, J. M. Liu, Y. Lyu, H. C. Wu, S. Yuan, R. Hai, C. Li, C. L. Feng, D. Y. Zhao and H. B. Ding, *J. Anal. At. Spectrom.*, 2021, **36**, 1159–1169.

19 H. Shin, J. Hwang, Y. Han, G. Shin, H. Lee, K. B. Chai and W. Choe, *Nucl. Fusion*, 2023, **63**, 044003.

20 N. Asakura, T. Nakano, O. Naito and N. Oyama, *J. Nucl. Mater.*, 2011, **415**, S318–S321.

21 K. D. Li, Z. S. Yang, H. Q. Wang, G. S. Xu, Q. P. Yuan, H. Y. Guo, D. Eldon, A. L. Hyatt, D. Humphreys, M. W. Chen, K. Wu, J. B. Liu, T. He, Q. Q. Yang, X. Lin, J. C. Xu, L. Y. Meng, F. Ding, X. H. Chen, Y. Luo, J. H. Wu, Y. M. Duan, G. N. Luo and L. Wang, *Nucl. Fusion*, 2021, **61**, 066013.

22 K. Li, X. Lin, Z. Yang, Q. Yang, G. Xu, L. Meng, Y. Wang, H. Lan, B. Zhang, L. Xu, K. Wu, T. He, J. Xu, J. Wu, F. Ding, Y. Duan, S. Mao, Q. Zang, L. Zhang, T. Zhang, F. Wang, L. Wang and G. N. Luo, *Nucl. Fusion*, 2023, **63**, 026025.

23 S. I. Krasheninnikov, A. S. Kukushkin and A. A. Pshenov, *Phys. Plasmas*, 2016, **23**, 055602.

24 Y. Iida, *Spectrochim. Acta, Part B*, 1990, **45**, 1353–1367.

25 X. Mao, S.-b. Wen and R. E. Russo, *Appl. Surf. Sci.*, 2007, **253**, 6316–6321.

26 Y.-I. Lee, T. L. Thiem, G.-H. Kim, Y.-Y. Teng and J. Sneddon, *Appl. Spectrosc.*, 1992, **46**, 1597–1604.

27 F.-A. Barreda, F. Trichard, S. Barbier, N. Gilon and L. Saint-Jalmes, *Anal. Bioanal. Chem.*, 2012, **403**, 2601–2610.

28 W. Sdorra and K. Niemax, *Microchim. Acta*, 1992, **107**, 319–327.

29 A. Huber, B. Schweer, V. Philipps, N. Gierse, M. Zlobinski, S. Brezinsek, W. Biel, V. Kotov, R. Leyte-Gonzales, P. Mertens and U. Samm, *Fusion Eng. Des.*, 2011, **86**, 1336–1340.

30 Q. Xiao, R. Hai, H. Ding, A. Huber, V. Philipps, N. Gierse and G. Sergienko, *J. Nucl. Mater.*, 2015, **463**, 911–914.

31 A. Huber, B. Schweer, V. Philipps, R. Leyte-Gonzales, N. Gierse, M. Zlobinski, S. Brezinsek, V. Kotov, P. Mertens, U. Samm and G. Sergienko, *Phys. Scr.*, 2011, **2011**, 014028.

This journal is © The Royal Society of Chemistry 2025

J. Anal. At. Spectrom., 2025, **40**, 762–774 | **773**

32 V. Philipps, A. Malaquias, A. Hakola, J. Karhunen, G. Maddaluno, S. Almaviva, L. Caneve, F. Colao, E. Fortuna, P. Gasior, M. Kubkowska, A. Czarnecka, M. Laan, A. Lissovski, P. Paris, H. J. van der Meiden, P. Petersson, M. Rubel, A. Huber, M. Zlobinski, B. Schweer, N. Gierse, Q. Xiao and G. Sergienko, *Nucl. Fusion*, 2013, **53**, 093002.

33 M. Z. Tokar, N. Gierse, V. Philipps and U. Samm, *Nucl. Fusion*, 2015, **55**, 113017.

34 J. Oelmann, Z. H. Hu, C. Li, L. Y. Sun, J. M. Liu, F. Ding, L. Wang, S. Brezinsek, R. Ding, H. B. Ding, G. N. Luo, J. L. Chen and E. Team, *Fusion Eng. Des.*, 2021, **162**, 112108.

35 B. de Groot, G. J. van Rooij, V. Veremiyenko, M. G. von Hellermann, H. J. N. van Eck, C. J. Barth, G. L. Kruijtzer, J. C. Wolff, W. J. Goedheer, N. J. Lopes Cardozo, A. W. Kleyn, P. H. M. Smeets, S. Brezinsek, A. Pospieszczyk, R. A. H. Engeln and R. P. Dahiya, *Fusion Eng. Des.*, 2005, **74**, 155–159.

36 B. de Groot, R. S. Al, R. Engeln, W. J. Goedheer, O. G. Kruijt, H. J. v. d. Meiden, P. R. Prins, D. C. Schram, P. H. M. Smeets, V. P. Veremiyenko, W. A. J. Vijvers, J. Westerhout, A. W. Kleyn, N. J. L. Cardozo and G. J. van Rooij, *Fusion Eng. Des.*, 2007, **82**, 1861–1865.

37 G. J. van Rooij, V. P. Veremiyenko, W. J. Goedheer, B. de Groot, A. W. Kleyn, P. H. M. Smeets, T. W. Versloot, D. G. Whyte, R. Engeln, D. C. Schram and N. J. L. Cardozo, *Appl. Phys. Lett.*, 2007, **90**, 121501.

38 Y. Wang, C. Li, J. L. Shi, X. W. Wu and H. B. Ding, *Plasma Sci. Technol.*, 2017, **19**, 115403.

39 M. Imran, S. Jielin, Z. Dongye, W. Qi, W. Yong, L. Cong, H. Ran, H. Sattar, M. Zhongxin, W. Wan-Jing, L. Guang-Nan, G. Remnev and D. Hongbin, *High Temp. Mater. Processes*, 2017, **21**, 277–288.

40 D. U. B. Aussems, D. Nishijima, C. Brandt, R. P. Doerner and N. J. L. Cardozo, *J. Appl. Phys.*, 2014, **116**, 063301.

41 D. Nishijima and R. P. Doerner, *J. Phys. D: Appl. Phys.*, 2015, **48**, 325201.

42 A. Ciucci, M. Corsi, V. Palleschi, S. Rastelli, A. Salvetti and E. Tognoni, *Appl. Spectrosc.*, 1999, **53**, 960–964.

43 D. W. Hahn and N. Omenetto, *Appl. Spectrosc.*, 2010, **64**, 335A–366A.

44 V. Morel, A. Bultel, I. Schneider and C. Grisolia, *Spectrochim. Acta, Part B*, 2017, **127**, 7–19.

45 S. Eschlböck-Fuchs, M. J. Haslinger, A. Hinterreiter, P. Kolmhofer, N. Huber, R. Rössler, J. Heitz and J. D. Pedarnig, *Spectrochim. Acta, Part B*, 2013, **87**, 36–42.

46 V. N. Lednev, M. Y. Grishin, P. A. Sdvizhenskii, R. D. Asyutin, R. S. Tretyakov, A. Y. Stavertiy and S. M. Pershin, *J. Anal. At. Spectrom.*, 2019, **34**, 607–615.

47 Z. L. He, X. Y. Wang, R. Hai, X. Bai, D. Wu, H. Wu, W. N. Tong, C. Li, Q. Wang and H. B. Ding, *Spectrochim. Acta, Part B*, 2022, **197**, 106530.

48 H. Drawin, *Zeitschrift für Physik A Hadrons and nuclei*, 1969, **225**, 483–493.

49 X. M. Zhu and Y. K. Pu, *J. Phys. D: Appl. Phys.*, 2010, **43**, 015204.

50 V. Morel, A. Bultel, J. Annaloro, C. Chambrelan, G. Edouard and C. Grisolia, *Spectrochim. Acta, Part B*, 2015, **103–104**, 112–123.

51 I. Y. Tolstikhina, M. Imai and V. P. Shevelko, *Nucl. Instrum. Methods Phys. Res., Sect. B*, 2023, **535**, 241–246.

52 J. L. Weng, S. Kashiwakura and K. Wagatsuma, *Anal. Sci.*, 2021, **37**, 367–375.

53 V. I. Babushok, F. C. DeLucia, P. J. Dagdigian and A. W. Miziolek, *Spectrochim. Acta, Part B*, 2005, **60**, 926–934.

54 C. Fu, D. Wu, Q. Wang, L. Sun, Y. Wang and H. Ding, *J. Instrum.*, 2020, **15**, C02022.

55 S. S. Harilal, C. V. Bindhu, M. S. Tillack, F. Najmabadi and A. C. Gaeris, *J. Appl. Phys.*, 2003, **93**, 2380–2388.

56 V. Y. Baranov, O. Derkach, V. Grishina, M. Kanevskii and A. Y. J. P. R. E. Sebrant, *Phys. Rev. E:Stat. Phys., Plasmas, Fluids, Relat. Interdisc. Top.*, 1993, **48**, 1324.

774 | *J. Anal. At. Spectrom.*, 2025, **40**, 762–774

This journal is © The Royal Society of Chemistry 2025